Simulating landslides using two-phase two-point material point method

Zhiqi Zhan[1], and *Chao* Zhou[1*]

[1]Department of Civil and Environmental Engineering, The Hong Kong Polytechnic University, Hung Hom, Kowloon, Hong Kong

Abstract. Material point method (MPM) is an effective numerical method for large-deformation analysis under unsaturated conditions. In the previous studies, water retention ability and permeability function were assumed to be independent of soil deformation. Besides, most studies used a single set of material points, so some processes (e.g., the infiltration of free water into unsaturated soil) cannot be modelled. Thereby, a two-point MPM approach has been extended from saturated to unsaturated soils. The required information of solid and liquid phases is carried by two individual sets of material points, with the assumption of zero pore air pressure. GIMP is applied for space discretisation. In the modelling of hydraulic behaviour, the porosity-dependency of the water retention curve and permeability function are incorporated. A centrifuge test about rainfall-induced unsaturated soil slope failure is simulated to investigate the influence of the porosity-dependent water retention curve and permeability function. Parametric studies demonstrate soil parameters for water retention behaviour and shear strength play significant roles in the slope failure mechanisms.

1 Introduction

Many geotechnical problems involve large deformations, which cannot be easily reproduced by using the finite element method (FEM) because of mesh distortion. Some mesh-free numerical methods such as the material point method (MPM) offer an effective solution. The MPM approach is an improved particle-in-cell (PIC) method where the Lagrangian (Lagrangian point masses) and Eulerian (Eulerian background mesh) descriptions are both applied [1].

So far, the MPM has been applied to model a number of problems. Most of the previous studies focused on saturated soils, which is a two-phase material comprising solid particles and liquid waters, with two distinct schemes (i.e., representing saturated soils using one set or two sets of material points).

For two-phase one-point scheme, a single set of Lagrangian material points is used to represent the solid (i.e., soil particles) and liquid phases (i.e., pore water). Zhang et al. [2] proposed a coupling MPM based on the $\boldsymbol{u}^s - p^l$ form governing equations to solve dynamic responses of fully saturated soils, where $\boldsymbol{u}^s$ is the displacement of solid phase and p^l is the liquid pressure. Alonso and Zabala [3] simulated Aznalcollar dam failure by a $\boldsymbol{u}^s - p^l$ formulation. In the $\boldsymbol{u}^s - p^l$ formulation, two mesh size-related step criteria should be satisfied because of the different primary unknowns for the solid and liquid phases [4]. For a small-size mesh, the second compression wave cannot be captured accurately because the p^l-dependendt time step is too short [5]. Therefore, Jassim et al. [6] developed a two-phase one-point MPM with the $\boldsymbol{u}^s - \boldsymbol{u}^l$ formulation, where $\boldsymbol{u}^l$ is the displacement of the liquid phase.

Two-phase one-point MPM formulation is computationally efficient. However, it is not applicable to many engineering problems, like rainfall-induced ponding and internal erosion. Besides, it is unsuitable for problems with a high relative acceleration between the liquid and solid [7]. Hence some researchers have adopted the two-phase two-point scheme. Abe et al. [8] proposed a two-phase two-point MPM to simulate a river levee embankment failure example by $\boldsymbol{u}^s - p^l$ formulation. Bandara and Soga [9] extended $\boldsymbol{u}^s - \boldsymbol{u}^l$ formulation [6] to two-phase two-point material point method, in which the relative acceleration between liquid and solid was considered. Based on the work of Bandara & Soga [9], Liu et al. [10] developed a three dimensional two-phase two-point MPM code, and the generalized interpolation material point method (GIMP) was used for spatial discretization.

In recent years, the MPM was also applied to simulate unsaturated soils. Similar to the modelling of saturated soils, several schemes have been proposed for unsaturated soils. Higo et al. [11] proposed an MPM-FDM coupled numerical method for the saturated and unsaturated soils, and the $\boldsymbol{u}^s - p^l$ form governing equations was applied. Yerro et al. [12] followed the research of $\boldsymbol{u}^s - \boldsymbol{u}^l$ formulation [6], developed a one-point three-phase MPM approach for unsaturated soils simulation. The momentum balance of solid, liquid and gas were all adapted to govern the motion of them.

* Corresponding author: c.zhou@polyu.edu.hk

© The Authors, published by EDP Sciences. This is an open access article distributed under the terms of the Creative Commons Attribution License 4.0 (http://creativecommons.org/licenses/by/4.0/).

Alternatively, some researchers [13-15] neglected the gas density and gas pressure, analysed the failure and post-failure process of unsaturated soil slope by the simplified one-point two-phase MPM, which is in $\boldsymbol{u}^s - \boldsymbol{u}^l$ formulation. For the simulation of dynamic interaction of free water and soils, Feng et al. [16] proposed a hydro-mechanically coupled two-phase two-point MPM for saturated and unsaturated soils.

This study extends the research of Zhan et al., [17], modelled the unsaturated landslide by a two-phase two-point MPM approach. The proposed MPM formulation is suitable for solving large deformation problems involving saturated and unsaturated soils. Gas density and pressure are not considered. The generalised interpolation material point method (GIMP) is adopted for space discretisation to minimise the numerical oscillations during computation. The governing equations and stabilization technique are introduced in the following sections. A centrifuge test about rainfall-induced slopes instability is simulated to highlight the influence of porosity change on the water retention curve and permeability function. Furthermore, parametric studies about the effect of soil water retention and shear strength parameters on the slope failure mechanisms are discussed as well.

For the symbol convention, for example, in $\dot{\boldsymbol{a}}_k^{\alpha}$, the superscript α can be s and l, representing the solid and water phases, respectively, and the variable without α is for the mixture; k means the time step k; the bold $\boldsymbol{a}$ means tensor; the dot is the time derivative. Regarding the sign convention, the tension in the solid phase and compression in the liquid phase are positive.

2 Governing equations

Unsaturated soil is a three-phase material comprising solid particles, liquid and gas. A comprehensive model should incorporate governing equations for all phases. However, the modelling of most geotechnical problems can be simplified, where the air in unsaturated soil is connected to the atmosphere and its pressure is maintained at zero. With this simplification, a two-phase two-point MPM approach is proposed for analyzing the hydro-mechanical geotechnical problems involving unsaturated soils.

In addition, the governing equations are based on the following assumptions: (i) soil particles are incompressible; (ii) the transfer of water vapor is negligible; (iii) the temperature is constant and uniform.

2.1 Momentum balance equations

The relative motion of liquid and solid phases can be considered in the two-phase two-point MPM. Two momentum balance equations are used to calculate the acceleration of liquid and solid phases.

For the liquid phase, the momentum balance is as follows:

$$\rho^l \dot{\boldsymbol{v}}^{\boldsymbol{l}} = \boldsymbol{F}_d^l - \nabla p^l + \rho^l \boldsymbol{g} \quad (1)$$

where ρ^l is the density of the liquid phase, $\dot{\boldsymbol{v}}^{\boldsymbol{l}}$ is the acceleration of the liquid phase, $\boldsymbol{g}$ is the gravitational acceleration, and $\boldsymbol{F}_d^l$ is the drag force imposed by the solid-fluid interaction.

The drag force is governed by Darcy's law when a laminar and steady flow in a low-velocity regime is simulated:

$$\boldsymbol{F}_d^l = -\frac{nS_r\rho^l g}{k}(\boldsymbol{v}^l - \boldsymbol{v}^s) \quad (2)$$

where n is the porosity, S_r is the degree of saturation, $\boldsymbol{v}^{\boldsymbol{l}}$ is the velocity of the liquid phase, $\boldsymbol{v}^s$ is the velocity of the solid phase, k is the permeability.

The solid-fluid mixture needs to meet both linear and angular momentum balances. Since the tensor of total stress $\boldsymbol{\sigma}$ is symmetric, the angular momentum is always fulfilled. The linear momentum balance is described by

$$(1-n)\rho^s \dot{\boldsymbol{v}}^s + nS_r\rho^l \dot{\boldsymbol{v}}^l = div(\boldsymbol{\sigma}) + (1-n)\rho^s \boldsymbol{g} + nS_r\rho^l g \quad (3)$$

where ρ^s is the density of the solid phase (i.e., soil particles), $\dot{\boldsymbol{v}}^s$ is the acceleration of the solid phase.

From the above momentum balance equations for the liquid and solid-fluid mixture, the velocity of liquid and solid phases can be obtained.

2.2 Mass balance equations

The mass balance of the solid phase is given by

$$\frac{\partial}{\partial t}[\rho^s(1-n)] + div[\rho^s(1-n)\boldsymbol{v}^s] = 0 \quad (4)$$

By assuming that soil particles are incompressible ($\frac{\partial \rho^s}{\partial t} \approx 0$ and $\nabla \rho^s \approx 0$), Eq. (4) is reduced to Eq. (5):

$$\frac{\partial n}{\partial t} = (1-n)\, div(\boldsymbol{v}^S) - \boldsymbol{v}^S \nabla n \quad (5)$$

Similarly, the mass balance of the liquid phase is given by the following equation:

$$\frac{\partial}{\partial t}(nS_r\rho^l) + div(nS_r\rho^l \boldsymbol{v}^l) = 0 \quad (6)$$

The gradient of the water density is negligible ($\nabla \rho^l \approx 0$) for water is only weakly compressible. In addition, $\frac{1}{\rho^l}\frac{\partial \rho^l}{\partial p^l} = \frac{1}{K^l}$, where K^l is the compressibility of the liquid phase. The following equation can be therefore derived based on Eq. (7):

$$n\left(\frac{S_r}{K^l} + \frac{\partial S_r}{\partial p^l}\right)\frac{\partial p^l}{\partial t} + S_r\frac{\partial n}{\partial t} + nS_r\, div(\boldsymbol{v}^l) + \boldsymbol{v}^l \nabla n S_r = 0 \quad (7)$$

Substituting Eq. (5) into Eq. (7), it is obtained that:

$$n\left(\frac{S_r}{K^l} + \frac{\partial S_r}{\partial p^l}\right)\frac{\partial p^l}{\partial t} = -S_r\left[(1-n)\, div(\boldsymbol{v}^S) - \boldsymbol{v}^S \nabla n + n\, div(\boldsymbol{v}^l) + \boldsymbol{v}^l \frac{\nabla n S_r}{S_r}\right] \quad (8)$$

Eq. (8) can update the pore water pressure under both saturated and unsaturated conditions.

2.3 Constitutive equations for the mechanical behaviour

The Bishop's stress is applied in this study:

$$\boldsymbol{\sigma}^* = \boldsymbol{\sigma} + \chi p^l \boldsymbol{\delta} \quad (9)$$

where $\boldsymbol{\sigma}^*$ is the Bishop's stress tensor, χ is the Bishop parameter, and it is simplified as S_r, $\boldsymbol{\delta}$ is the Kronecker delta function. In the fully saturated condition, the Bishop's stress reduces to Terzaghi's effective stress.

Using Bishop's stress, the Drucker–Prager model with strain hardening/softening is used to model the behaviour of saturated and unsaturated soils. Details of

this method were reported by Bandara and Soga [9]. It should be pointed out that only the shear strength evolution can be simulated using the Drucker–Prager model in combination with Bishop's stress, while other affects such as collapse upon wetting cannot be simulated due to the lack of a loading collapse surface. However the results are justified due to the physical problem simulated (slope failure) which is primarily related to shear strength reduction due to water saturation and pore pressure build up.

Apart from the stress state variables and the incorporation of strain hardening/softening, all other mathematical formulations from the Drucker–Prager model can be equally applied here. Since details of the Drucker–Prager model are widely reported in the literature, they are not repeated here. In the extended Drucker–Prager model, the stress-strain relation is given by

$$d\boldsymbol{\sigma}^* = \boldsymbol{D}^{ep} d\boldsymbol{\varepsilon} \tag{10}$$

where $\boldsymbol{\varepsilon}$ is the strain, and $\boldsymbol{D}^{ep}$ is the stiffness tensor.

2.4 The Constitutive equations for the hydraulic behaviour

Soil water retention curve (SWRC) is important in modelling unsaturated soil behaviour [18]. The current study adopts the SWRC model of Tarantino [19], which is developed from van Genuchten's [20] model by incorporating the influence of void ratio. The relationship between the effective degree of saturation (S_{eff}) and pore water pressure is described as follows:

$$S_{eff} = \frac{S_r - S_{res}}{1 - S_{res}} = \left[1 + \left(a \frac{se^b}{\rho^l g}\right)^{\frac{1}{1-\lambda}}\right]^{-\lambda} \tag{11a}$$

where

$$e = \frac{\mathrm{n}}{1-n} \tag{11b}$$

$$b = \frac{1-\lambda}{\lambda} \tag{11c}$$

where S_{res} is the residual degree of saturation, s is the matric suction, a and λ are model parameters related to the pore size distribution of soil, e is the void ratio, b is a parameter describing void ratio effects on the water retention behaviour.

On the other hand, the water permeability k of unsaturated soil is modelled by the following equation:

$$k = k_{sat} k_r \tag{12}$$

where k_{sat} is the saturated permeability, k_r is the relative permeability for describing the influence of unsaturation on water permeability. The method of Mualem [21] is used to determine the relationship between k_r and the effective degree of saturation:

$$k_r = \sqrt{S_{eff}} \left[1 - \left(1 - S_r^{\frac{1}{\lambda}}\right)^{\lambda}\right]^2 \tag{13}$$

In addition, k_{sat} varies with porosity [22]:

$$k_{sat} = C \frac{n^3}{(1-n)^2} \tag{14}$$

where C is a soil parameter. Eqs. (11) to (14) suggest that the SWRC, relative permeability and saturated permeability are affected by porosity.

3 Numerical implementation

Detail about space discretisation of momentum balance equations, time discretisation and computational procedures are reported by Zhan et al. [17], so they are not repeated in this paper. This section focuses more on stabilization technique for proposed MPM formulation.

The generalised interpolation material point method (GIMP) [23] is applied in this study for space discretisation. In GIMP, a smooth weight function is adapted instead of an unsmooth shape function. Therefore, GIMP shows a better capability of minimising numerical oscillations than the standard MPM.

Besides, multiple criteria for the critical time step should be considered to achieve a stable solution for the multi-phase MPM formulations [24]. To achieve a convergent solution, the critical computational time step is derived by taking the smaller value of the permeability-dependent criterion [25] and the Courant-Friedrichs-Levy (CFL) condition [26].

4 MPM simulation of rainfall-induced failure of an unsaturated sand slope

The detail of verification of MPM formulation has been reported by Zhan et al. [17]. This paper follows a simulation of Zhan et al. [17], which is a centrifuge model test reported by Wang et al. [27], to investigate the soil parameters of water retention behavior and shear strength effect on slope failure mechanisms.

Fig. 1 shows the geometry of soil slope in the MPM model, consistent with the test condition of Wang et al. [27]. The slope height equals 200 mm, and the slope angle is 45°. The test and numerical simulations were finished at 30-g, so the slope height is 6 m at the prototype scale. The cell size equals $10\ \mathrm{mm} \times 10\ \mathrm{mm} \times 10\ \mathrm{mm}$, and there are eight material points for each phase in one cell.

Regarding the boundary conditions, the ground surface is permeable and free to move. The heavy rainfall condition is simulated by maintaining zero suction at the ground surface after an equilibrium state is achieved at the prescribed g-level ((initial water content $w_0 = 11.5\%$). The lateral boundaries are impermeable and fixed for horizontal displacement. The bottom boundary is impermeable, and no displacement is allowed in any direction.

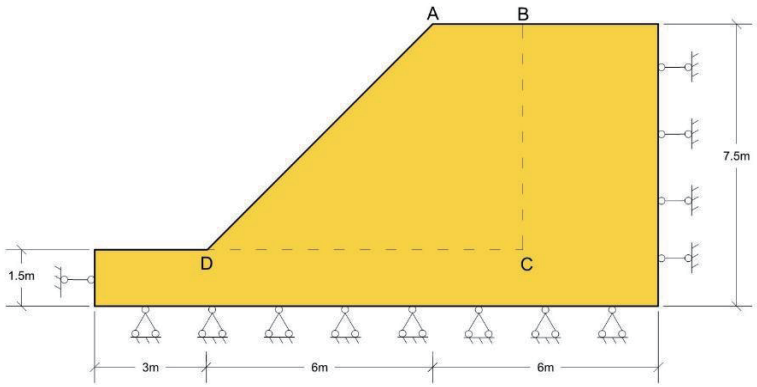

Fig. 1. Geometry and boundary conditions of the model used in GIMP (the displacement in Zone ABCD was measured during the test).

4.1 Influence of water retention and shear strength parameters

The soil used to simulation is classified as well-graded silty sand with loose ($n = 0.48$, $k_{sat} = 2.77 \times 10^{-3}$ m/s) and dense ($n = 0.34, k_{sat} = 2 \times 10^{-5}$ m/s) compaction state. The triaxial tests of Wang et al. [27] are used to calibrate shear strength and water retention parameters. Constant shear strength parameters of the soil are $\varphi = 31.8°$ and $c = 0$ kPa for the loose state and $\varphi = 38.1°$ and $c = 15$ kPa for the dense state. For water retention parameters, $a = 1.2$, $\lambda = 0.89$ and $S_{res} = 0$ for the loose state, while $a = 1.76, \lambda = 0.66$ and $S_{res} = 0$ for the dense state. In addition, there is a volumetric contraction for the silty sand at a loose state, while a dilatancy is observed at a dense state. Therefore, a negative dilation angle ($\psi^{peak} = -5°$) and a positive dilation angle ($\psi^{peak} = 5°$) are applied to simulate strain-hardening and strain-softening for loose and dense sand, with $\gamma^{peak} = 0.01$ and $\gamma^{crit} = 0.2$. And other typical parameters shown in Table 1 are adapted for both loose and dense sand.

Table 1. Material characteristics for centrifuge model test

Water bulk modulus, K^l	2.2 GPa
Solid density, ρ^s	2670 kg/m3
Water density, ρ^l	1000 kg/m3
Solid Young's modulus, E	10 MPa
Poisson's ratio, ν	0.33

For parametric studies, Fig. 2 (b) and (d) show the results of displacement at four different times: $t_1 = 10$ s, $t_2 = 20$ s , $t_3 = 30$ s , $t_4 = 40$ s of loose and dense soil. Large displacement mainly occurs at the upper part of the slope (i.e., Zone ABCD in Fig. 1, and the maximum displacement is located at the slope crest. In this section, the porosity dependency of hydraulic properties is not considered, a constant void ratio is used for Eq. (11) and (14). For silty sand with loose state, the displacement is smaller compared with dense state. According to SWRC, dense sand has a higher water retention ability, so a higher equilibrium suction is predicted at a same degree of saturation, which means a higher value of Bishop's effective stress and lower relative permeability. Dense sand also has a higher shear strength. In addition, dense sand has a smaller amount of rainfall infiltration because of a smaller value of permeability.

4.2 Influence of porosity dependency SWRC and permeability function

Fig. 2 (a) and (b) are displacement contours of loose and dense sand involving influence of porosity on Eq. (11) and (14). The reason of difference between Fig. 2 (a) and (b) has been reported by Zhan et al. [17]. And as it is shown in Fig. 2 (c) and (d), when the porosity dependency of SWRC and permeability function is considered, the displacement is larger. It is mainly because the dense sand shows dilatancy behaviour [22] during the process of slope deformation. When the porosity dependent SWRC are considered through Eq. (14), the soil is expected to have a lower water retention ability. Consequently, a lower equilibrium suction is predicted at a given degree of saturation, leading to higher relative permeability and lower strength. Moreover, there is an increase in saturated permeability when porosity effects are included in Eq. (14), resulting in a larger amount of rainfall infiltration and, therefore, there is a larger slope displacement.

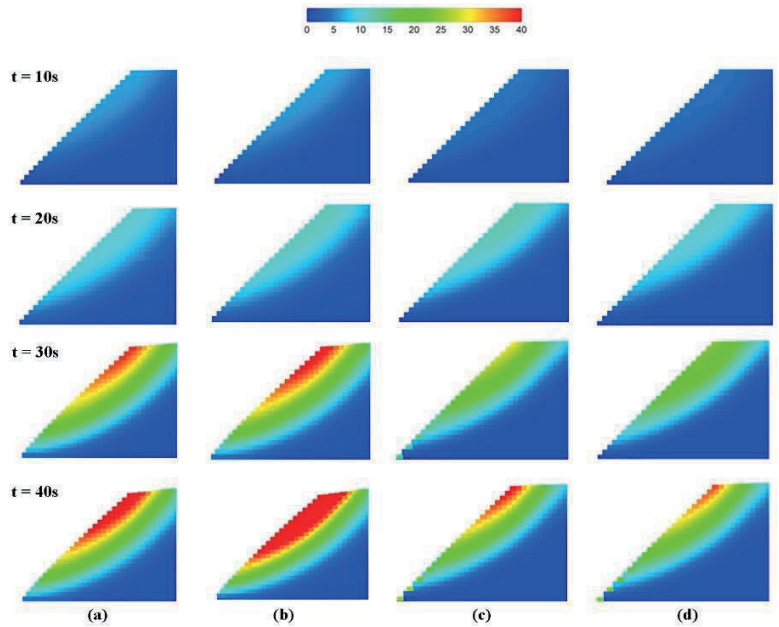

Fig. 2. MPM results of pre-failure soil displacement (unit: mm) in Zone ABCD when the unsaturated sand slope is subjected to rainfall (a) loose sand considering porosity effects on SWRC and permeability function; (b) loose sand with constant SWRC and permeability function for loose sand; (c) dense sand MPM considering porosity effects on SWRC and permeability function; and (b) dense sand with constant SWRC and permeability function for dense sand.

Fig. 3 shows the post-failure of dense soil displacement. The slope failure occurs at $t = 60\ s$ with a maximum displacement value of 40 mm. The top part of the slope continues moving down from $t = 70\ s$ to $t = 100\ s$, and the average depth of the sliding Zone is about 0.7 m at the prototype scale. There is a loss of suction because of rainfall-infiltration, according to Eq. (9), the Bishop's stress decreases and slope failure occurs. The post-failure of loose soil displacement can be referred to Zhan et al. [17].

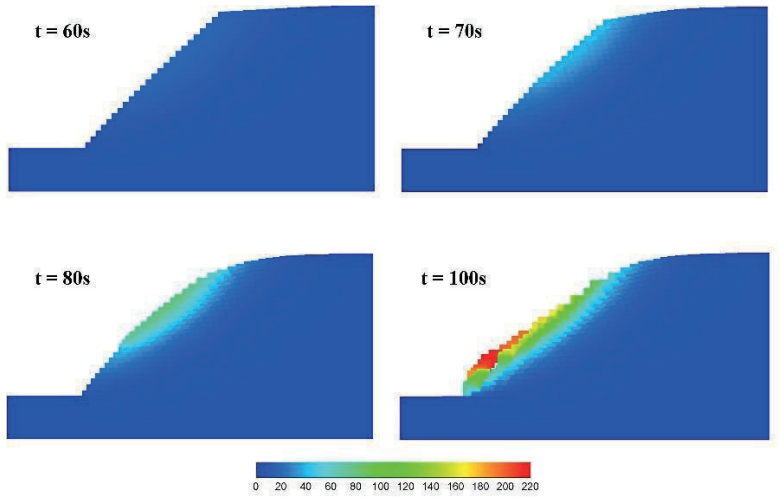

Fig. 3. Post-failure soil displacement (unit: mm) at four different times calculated using MPM.

5 Summary and Conclusions

In this study, a two-phase two-point MPM formulation is developed for the coupled hydro-mechanical behaviour of saturated and unsaturated soils. The proposed MPM formulation has newly incorporated the influence of porosity on the water retention ability and permeability function. For spatial discretisation, GIMP is applied for minimum numerical oscillations.

The rainfall-induced failure of unsaturated soil slope was simulated to evaluate the new code for analysing large deformation problems involving unsaturated soils. Parametric studies demonstrate soil water retention and shear strength parameters play significant roles on the slope failure mechanisms. Besides, for dense sand, when the influence of porosity on SWRC and permeability function is not considered, the displacement is underestimated.

Acknowledgements

This work is supported by the Research Grants Council (RGC) of the HKSAR through the research grants 16207918 and 15205721.

References

1. D. Sulsky, Z. Chen, and H. L. Schreyer, Computer methods in applied mechanics and engineering **118** (1-2), 179 (1994).
2. H. Zhang, K. Wang, and Z. Chen, Computer methods in applied mechanics and engineering **198** (17-20), 1456 (2009).
3. E. E. Alonso, N. M. Pinyol, and A. M. Puzrin, *Geomechanics of failures: advanced topics*. (Springer, 2010).
4. A. Verruijt, *An introduction to soil dynamics*. (Springer Science & Business Media, 2009).
5. J. Van Esch, D. Stolle, and I. Jassim, presented at the 2nd International Symposium on Computational Geomechanics, 2011 (unpublished).
6. I. Jassim, D. Stolle, and P. Vermeer, International journal for numerical and analytical methods in geomechanics **37** (15), 2502 (2013).
7. O. C. Zienkiewicz, A. Chan, M. Pastor, D. Paul, and T. Shiomi, Proceedings of the Royal Society of London. A. Mathematical and Physical Sciences **429** (1877), 285 (1990).
8. K. Abe, K. Soga, and S. Bandara, Journal of Geotechnical and Geoenvironmental Engineering **140** (3), 04013033 (2014).
9. S. Bandara and K. Soga, Computers and geotechnics **63**, 199 (2015).
10. C. Liu, Q. Sun, F. Jin, and G. G. Zhou, Powder technology **314**, 110 (2017).
11. Y. Higo, F. Oka, S. Kimoto, Y. Morinaka, Y. Goto, and Z. Chen, Soils and foundations **50** (4), 515 (2010).
12. A. Yerro, E. Alonso, and N. Pinyol, Géotechnique **65** (3), 201 (2015).
13. B. Wang, P. Vardon, and M. Hicks, Engineering Geology **239**, 1 (2018).
14. X. Lei, S. He, X. Chen, H. Wong, L. Wu, and E. Liu, Advances in Water Resources **141**, 103578 (2020).
15. F. Ceccato, A. Yerro, V. Girardi, and P. Simonini, Computers and Geotechnics **129**, 103876 (2021).
16. K. Feng, D. Huang, and G. Wang, Acta Geotechnica **16** (8), 2529 (2021).
17. Z. Zhan, C. Zhou, C. Liu, and C. Ng, Computers and Geotechnics **155**, 105224 (2023).
18. C. Zhou, P. S. So, and X. Chen, Journal of Hydrology **586**, 124874 (2020).
19. A. Tarantino, Géotechnique **59** (9), 751 (2009).
20. M. T. Van Genuchten, Soil science society of America journal **44** (5), 892 (1980).
21. Y. Mualem, Water resources research **12** (3), 513 (1976).
22. W. D. Carrier III, Journal of geotechnical and geoenvironmental engineering **129** (11), 1054 (2003).
23. S. G. Bardenhagen and E. M. Kober, Computer Modeling in Engineering and Sciences **5** (6), 477 (2004).
24. A. Yerro, V. Girardi, M. Martinelli, and F. Ceccato, Geomechanics for Energy and the Environment, 100343 (2022).
25. M. Mieremet, D. Stolle, F. Ceccato, and C. Vuik, International Journal for Numerical and Analytical Methods in Geomechanics **40** (9), 1284 (2016).
26. R. Courant, K. Friedrichs, and H. Lewy, IBM journal of Research and Development **11** (2), 215 (1967).
27. S. Wang, G. Idinger, and W. Wu, Acta Geotechnica **16** (9), 2899 (2021).